

Salzano, M., Lessard, M. R., Noh, S., Kim, H., Waters, C., Engebretson, M. J., Horne, R., Clilverd, M., Kadokura, A., Tanaka, Y., Kim, K., Matzka, J., Fromm, T., Goldstein, J., Kim, M. J. (2022): Modeling the Effects of Drift Shell Splitting in Two Case Studies of Simultaneous Observations of Substorm-Driven Pi1B and IPDP-Type EMIC Waves. - Journal of Geophysical Research: Space Physics, 127, 10, e2022JA030600.

<https://doi.org/10.1029/2022JA030600>

JGR Space Physics

RESEARCH ARTICLE

10.1029/2022JA030600

Key Points:

- Pi1Bs and IPDPs observed from Antarctic ground stations occur simultaneously with particle injections from substorm onset
- We simulate the trajectories of particle injections from substorm onset as subject to drift shell splitting across a full injection front
- Particle trajectories are dominated by injection boundary effects, but drift shell splitting affects the time-frequency features of IPDPs

Correspondence to:

M. Salzano and M. R. Lessard,
michelle.salzano@unh.edu;
marc.lessard@unh.edu












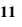
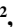

Citation:

Salzano, M., Lessard, M. R., Noh, S., Kim, H., Waters, C., Engebretson, M. J., et al. (2022). Modeling the effects of drift shell splitting in two case studies of simultaneous observations of substorm-driven Pi1B and IPDP-type EMIC waves. *Journal of Geophysical Research: Space Physics*, 127, e2022JA030600. <https://doi.org/10.1029/2022JA030600>

Received 29 APR 2022

Accepted 4 OCT 2022

Modeling the Effects of Drift Shell Splitting in Two Case Studies of Simultaneous Observations of Substorm-Driven Pi1B and IPDP-Type EMIC Waves

Michelle Salzano¹ , Marc R. Lessard¹ , Sungjun Noh^{2,3} , Hyomin Kim² , Colin Waters⁴ , Mark J. Engebretson⁵ , Richard Horne⁶ , Mark Clilverd⁶ , Akira Kadokura^{7,8,9} , Yoshimasa Tanaka^{7,8,9} , Khan-Hyuk Kim¹⁰ , Jürgen Matzka¹¹ , Tanja Fromm¹², Jerry Goldstein^{13,14} , and Myeong Joon Kim¹⁴ 

¹Space Science Center, University of New Hampshire, Durham, NH, USA, ²Center for Solar-Terrestrial Research, New Jersey Institute of Technology, Newark, NJ, USA, ³Los Alamos National Laboratory, Los Alamos, NM, USA, ⁴University of Newcastle, Callaghan, New South Wales, Australia, ⁵Physics Department, Augsburg College, Minneapolis, MN, USA, ⁶British Antarctic Survey (UKRI-NERC), Cambridge, UK, ⁷National Institute of Polar Research, Midori-cho, Tachikawa-shi, Japan, ⁸Polar Environment Data Science Center, Joint Support-Center for Data Science Research, Research Organization of Information and Systems, Midori-cho, Tachikawa, Japan, ⁹The Graduate University for Advanced Studies (SOKENDAI), Midori-cho, Tachikawa-shi, Japan, ¹⁰School of Space Research, Kyung Hee University, Yongin-si, South Korea, ¹¹GFZ German Research Center for Geosciences, Potsdam, Germany, ¹²Alfred Wegener Institut, Bremerhaven, Germany, ¹³Space Science and Engineering Division, Southwest Research Institute, San Antonio, TX, USA, ¹⁴Department of Physics and Astronomy, University of Texas, San Antonio, TX, USA

Abstract Intervals of pulsations of diminishing periods (IPDPs) are a subtype of electromagnetic ion cyclotron (EMIC) waves that can be triggered by substorm onset. Pi1B waves are ultralow frequency (ULF) broadband bursts that are well correlated with substorm onset. IPDPs are associated with increased fluxes of 40–60 keV substorm-injected protons which undergo gradient-curvature drifting and interact with the cold plasmasphere population. While particle trajectories and the generation of IPDPs have been modeled in the past, those models neglect the role that drift shell splitting plays in the process. This research investigates the different pathways that Pi1B and IPDPs take from their shared origin in substorm onset to their distinct observations on the ground, including the effects of drift shell splitting en route. This paper presents two case studies using data from an array of four ground-based Antarctic magnetometers that cover the evening sector, as well as in situ magnetometer data, proton fluxes, and proton pitch angles from the Van Allen Probes spacecraft. These observations identify a separation in geomagnetic latitude between Pi1Bs and IPDPs, and pinpoint a separation in magnetic local time (MLT). From these observations we model the drift shell splitting which injected particles undergo post-onset. This study shows that simulations that incorporate drift shell splitting across a full injection front are dominated by injection boundary effects, and that the inclusion of drift shell splitting introduces a slight horizontal component to the time axis of the time–frequency dependence of the IPDPs.

1. Introduction

Electromagnetic ion cyclotron (EMIC) waves are ultralow frequency (ULF) waves in the Pc1–2 band, where Pc1 encompasses 0.2–5 Hz frequencies and Pc2 encompasses 0.1–0.2 Hz frequencies (Jacobs et al., 1964). EMIC waves grow in amplitude via energy exchange with resonating ions. The free energy source is typically due to temperature anisotropy, which is the difference in the temperature of a plasma across the perpendicular and parallel components relative to the magnetic fields such that ($T_{\perp} > T_{\parallel}$) (Cornwall, 1965; Sagdeev & Shafranov, 1961; Usanova et al., 2014). In a uniform magnetic field, even weak temperature anisotropies drive instabilities in a plasma with non-Maxwellian velocity distributions, as charges in the tail of the velocity distribution come into cyclotron resonance (Sagdeev & Shafranov, 1961). EMIC waves tend to have an occurrence maximum in the dayside noon sector (Allen et al., 2015), although the research presented in the following sections focuses primarily on evening sector activity. A recent statistical study by Allen et al. (2015) used Cluster spacecraft data to establish three main generation regions for dusk sector EMIC waves: at low |MLAT| and high L-shells, EMIC waves are generated due to magnetopause compressions and drift shell splitting; off-equator, EMIC waves are generated due to Shabansky orbits; EMIC waves are also generated in regions where ring current H⁺ ions overlap cold

populations from the plasmasphere and plasmaspheric plumes. Additionally, in the absence of storms or compressions, Remya et al. (2018) used Van Allen Probes data to observe EMIC waves triggered by substorm-injected ions and found that the onset of the EMIC waves at probe A corresponded directly to injection times.

Similar to the EMIC waves discussed in Remya et al. (2018), intervals of pulsations of diminishing periods (IPDPs) are thought to be generated by ring current protons injected at substorm onset (Heacock, 1971; Horita et al., 1979; Søråas et al., 1980). IPDPs are a “rising tone” subtype of EMIC waves (not to be confused with chirping chorus waves, which can also have rising tones) that are characterized by an increase in frequency over time when observed from the ground. There have been a number of suggested mechanisms for the time–frequency characteristics of IPDPs. One of the earliest mechanisms suggested for this rising tone involves the westward drift mechanism along a given L shell, but that was found to not fully account for all events. Following this, an inward convection of the IPDP source region was suggested (Heacock, 1973). Koleszar (1988) considered three IPDP frequency change mechanisms, including inward convection, and found that inward motion was the dominating contributor to frequency change but that azimuthal drift also contributed. It is worth noting that the IPDP frequency change is typically not observed via in situ satellite measurement. This is possibly because in situ satellite measurements that occur at fixed L-values detect a constant frequency a few tenths of the local proton gyrofrequency (Søråas et al., 1980), but this does not account for higher latitudes where L-shell becomes less relevant nor does it account for satellite measurements that are not at fixed L. Because the IPDP frequency change mechanism is so complex, with multiple contributing factors, it remains worthy of study.

IPDPs are elliptically polarized (Bossen et al., 1976), and they are left (L) polarized when observed simultaneously with precipitation (Arnoldy & Lewis, 1979), which is useful both for identification of IPDPs and determining the latitude of the wave sources. It can be difficult to determine the latitude of source regions for waves due to ionospheric ducting, which is a process through which ULF Pc 1–2 waves will duct in the F_2 layer ionospheric waveguide (Kim et al., 2011; Neudegg et al., 2000). Waves that reach the ionosphere will duct in the direction of the Poynting flux $\vec{E} \times \vec{H}$. On the other hand, ducting makes it possible for ground stations to observe events they otherwise would not due to lack of spatial coverage. Ducting also allows them to observe a greater extent of conjugate events than is possible through in situ satellite measurements (Kim et al., 2010).

In some evening sector models of IPDP generation, protons injected at substorm onset will drift azimuthally westward and then undergo cyclotron instability in regions in or near the plasmopause, between 4.7 and 5.5 L shell (Heacock, 1971; Horita et al., 1979; Søråas et al., 1980). This is because protons must encounter regions of high cold plasma density for IPDPs to be generated, which they do as they cross the plasmopause into the plasmasphere (Kivelson & Russell, 1995; Maltseva et al., 1981). Additionally, the plasmopause is not the only place where these conditions can be met. An example is the plasmaspheric plume, which is a portion of the plasmasphere that extends beyond the plasmopause and can provide the necessary population (Chen & Wolf, 1972; Moldwin et al., 2004).

Particle motion in the magnetosphere will trace out three dimensional “drift shells.” In a purely dipolar field, particles of all pitch angles follow the same drift shell post-injection. However, the Earth’s magnetosphere isn’t a pure dipole—it is asymmetric and therefore introduces pitch angle dependence to particle trajectories. Drift shell splitting is the process by which particles with different pitch angles disperse radially (Roederer, 1967; Takahashi et al., 1997). It is possible that drift shell splitting may play a role in the movement of substorm-injected protons into suitable regions for the generation of IPDPs, which this research seeks to address.

Another relevant waveform is the Pi1B category. Pi1B waves are ULF broadband bursts in the Pi1 frequency range. First identified and differentiated as a subtype of Pi micropulsations in Heacock (1967), they are temporally short lived. Although Pi1B waves have a multitude of potential sources, they are well known to occur with substorm onset in the evening sector (Arnoldy et al., 1998). They have been identified both from the ground and at geosynchronous orbit. As suggested in Lessard et al. (2006); Lessard et al. (2011) and modeled in Pilipenko et al. (2008), Pi1B waves are believed to begin as compressional fast- (likely) or slow- (unlikely) mode waves at or beyond geosynchronous orbit. At this stage they are not constrained by the ambient magnetic field. Pi1B become increasingly parallel as they travel until they undergo a mode conversion into shear-mode waves. They then follow the field lines and propagate to the ionosphere. Finally, they contribute to the wave power that drives Alfvénic aurora at substorm onset.

Table 1
Ground Station Locations in Geographic and Geomagnetic Coordinates, As Well As Their Magnetic Midnights in UT and Their L-Shell Conjugacies

Station	Geo. Lat.	Geo. Long.	CGM Lat.	CGM Long.	MM	L
MAW	67.6 S	62.9 E	70.8 S	92.8 E	23:05	9.3
SYO	69.0 S	39.6 E	66.9 S	73.9 E	0:19	6.5
HBA	75.6 S	26.3 W	62.7 S	30.1 E	2:59	4.8
VNA	70.4 S	8.3 W	60.8 S	42.5 E	2:14	4.3

Note. Geomagnetic Coordinates and Magnetic Midnights Were Calculated for 01 January 2019 at 100 km Using AACGM-v2. L Shell Conjugacies Were Calculated Using IGRF.

IPDPs appear at lower geomagnetic latitudes (60–65°) than Pi1B waves, which are more prominent around 70° (Heacock, 1971). This relationship was observed in one of the case studies in Ranta et al. (1983), where Pi1B waves were observed at a higher geomagnetic latitude (63.7) than IPDPs (57.6). Ranta et al. (1983) speculated that the IPDPs, thought by Heacock (1971) to be caused by substorm-injected protons at the plasmopause, may indicate that precipitation occurs near the plasmopause region. Heacock (1971) speculated that there may also be a longitudinal difference between IPDPs and Pi1Bs, with Pi1Bs occurring in the near-midnight sector after substorm onset and IPDPs following in the afternoon–evening sector. Beyond this, published investigations into the relationship between IPDPs and Pi1B waves are relatively limited.

ULF waves play a significant role in radiation belt particle losses, both directly by inducing precipitation and indirectly by interacting with other waves that in turn cause losses. EMIC waves are of particular interest for the role they play in radiation belt dynamics (Brito et al., 2020). The following study demonstrates the role drift shell splitting plays in the generation and propagation of IPDPs. This is accomplished using two case studies that show the ground and space relationships between observed IPDPs and Pi1B ULF waves. Two models are described that simulate the drift shell splitting of substorm injected protons, one which uses a single injection point and one which encompasses a full injection boundary.

2. Data Sets

Ground magnetometer data were obtained from an array of four ground stations located in Antarctica: Halley Research Station (HBA), Neumayer III (VNA), Syowa (SYO), and Mawson (MAW). Their station coordinates, magnetic midnights, and conjugate L-shells are listed in Table 1. All four stations have a system of searchcoil magnetometers (also known as induction magnetometers) that consist of two orthogonal sensors that measure magnetic flux in nT/s. The sensors at HBA, VNA, and MAW are aligned geomagnetically South (X) and East (Y), while the sensors at SYO are aligned geomagnetically North (X) and East (Y). The sensors at HBA and VNA are orthogonal to the field line while the sensors at MAW and SYO are level in the orthogonal plane. The sensors located at HBA, VNA, and SYO sample at 20 Hz, which is ideal for observing EMIC waves. The searchcoil located at MAW samples at 2 Hz—sufficient for identifying Pi1B waves. Searchcoil magnetometers are chosen over fluxgate magnetometers because fluxgates typically lack the appropriate sensitivity to fully observe EMIC waves. More information about how these searchcoils operate can be found in Kim (2010).

Spacecraft data are obtained from three instruments aboard the Van Allen Probes spacecraft, which are a set of two spacecraft that carry instruments designed to study the ring current and radiation belt particles. The instruments used in this study are the Electric and Magnetic Field Instrument Suite and Integrated Science (EMFISIS) instrument suite, the Radiation Belt Storm Probes Ion Composition Experiment (RBSPICE) instrument, and the Helium, Oxygen, Proton, and Electron (HOPE) mass spectrometer. EMFISIS is composed of a tri-axial fluxgate magnetometer and a tri-axial searchcoil magnetometer, and is used in this study to observe EMIC and Pi1B waves. RBSPICE uses a time-of-flight versus energy spectrometer to measure H⁺, He⁺, and O⁺ ions as well as protons and electrons, and is used in this study to identify proton and ion injections between 45 and 598 keV during substorms. HOPE is a plasma spectrometer that measures in situ plasma ion and electron fluxes for energies between 1 eV and 50 keV, and is used in this study for completeness at lower energies. In the first case study on 27 February 2019, Van Allen Probe A is positioned optimally in the evening sector near the plasmatail. In the second case study on 7 March 2019, Van Allen Probe B is positioned optimally in the evening sector near the plasmatail.

Data from riometers located at HBA and MAW, an imaging riometer located at SYO, and a vector field magnetometer located onboard the low earth orbiting satellite SWARM were also investigated, though they are not published or discussed here.

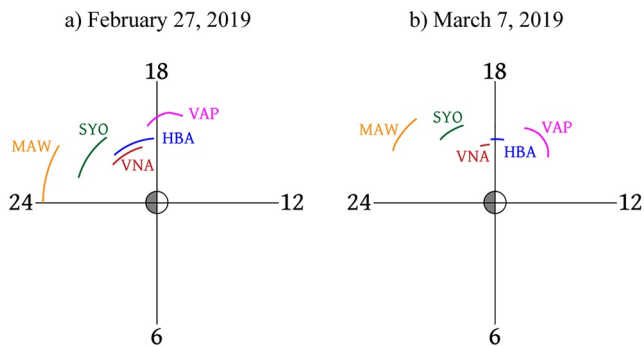


Figure 1. Magnetic local time (MLT) clocks illustrating the approximate spatial coverage at each ground station as well as the Van Allen Probes for (a) 27 February 2019 and (b) 7 March 2019. For particles injected at the nightside, we expect the events to be observed first by MAW (yellow), followed by SYO (green), VNA (red), HBA (blue) and finally the Van Allen Probes (pink). The use of these colors is merely to help distinguish the stations visually. The radial distance of each line from the center of the plot is reflective of increasing L shell conjugacy (or in the case of the Van Allen Probes, in situ location).

3. Observations

This section describes two case studies of events involving simultaneous observations of IPDPs and Pi1B waves that occurred during substorm onset. The events chosen for these case studies fit four criteria: (a) There are ground observations of IPDPs; (b) There are near-simultaneous ground observations of Pi1Bs; (c) There are space observations of proton injections during substorm onset; and (d) The events occur during relatively quiet periods without other complicating factors. The first case study occurred over 2100–2400 UT on 27 February 2019, heretofore referred to as the February event. The second case study occurred over 2015–2115 UT on 7 March 2019, heretofore referred to as the March event. The magnetic local time (MLT) coverage is in the evening sector for both events as shown in Figure 1. The February event reaches magnetic midnight, while the March event occurs slightly earlier and remains confined to the evening sector. Substorm proton injections are observed by the Van Allen probes for both events.

Magnetometer time series data were converted into spectrograms via FFT methods. IPDPs (characterized by an increase in frequency over tens of minutes in the Pc1 band) and Pi1B waves (characterized by short lived broadband bursts in the Pi1 band) are identified visually from the spectrograms.

There was a minor amount of uncertainty involved due to the choice of spectrogram parameters, such as the size of the sliding window and the number of FFTs to perform, but this mainly affects timing on the order of seconds. A more quantitative analysis would be required to compare onset times at this level of confidence, but it is not a problem for the purposes of this paper. For the plots shown here, a sliding window of between 1 and 30 data points was used. NFFT, which is an integer of 2^n that approximates the signal length to transform and affects the resolution of the resulting spectrogram, was set to 2048. This corresponds to roughly 102.4 s of data for the 20 Hz stations and 1,024 s of data for the 2 Hz station. The log power scale, which affects color intensities and can be adjusted to select events, was fixed from -0.7 to -4.7 . Events were identified at log powers larger than approximately -3.7 .

The spectrograms for the February event are shown in Figure 2a. IPDPs are observed at lower latitudes (60.8° and 62.7° S) than Pi1B waves (66.9° and 70.8° S), and the Pi1B observations slightly lead the IPDP observations. The polarization analysis of the searchcoil magnetometer data, shown in Figure 2b, is based on the methods described by Rankin and Kurtz (1970) and Fowler et al. (1967). Blue (negative) corresponds to left polarization and red (positive) corresponds to right polarization. The polarization is not shown for Syowa station as the methods used to determine the polarization for the other stations were not sufficient to distinguish wave forms at Syowa.

The IPDP taken as a whole lasted approximately 2.5 hr. This event can be divided into four intervals of distinct IPDP signatures with the help of the polarization analysis. Interval 1 lasted from 2112 to 2200 UT. Interval 2 lasted from 2200 to 2230 UT. Interval 3 lasted from 2230 to 2306 UT. Interval 4 lasted from 2300 to 2324 UT. Interval 2 was chosen as the main IPDP for this case study. Across interval 2, the frequency increased from 0.1 to 0.85 Hz, a frequency change of approximately 0.025 Hz/min.

Spectrograms for the March event are shown in Figure 3 and are more straightforward than the February event. The time scale for this event (approximately 30 min) is comparable to a single sub-IPDP in the February event. Once again the higher latitude Pi1B measurements lead the lower latitude IPDP observations by minutes. The IPDP rises from 0.2 to 0.6 Hz between 2050 UT and 2116 UT, a frequency change of approximately 0.015 Hz/min. There is an interesting change in polarization over frequency in Figure 3b seen from VNA.

The observations of the Pi1B waves in Figures 2 and 3 are important in the context of tying the ground observations to substorms. Pi1B waves are well correlated with substorm onset, so the simultaneous observation of Pi1Bs and IPDPs indicates that the IPDPs may also be tied to substorm onset, even before considering space observations. The Pi1B waves also help to time substorm onset in a way that can be difficult from only in situ space observations. While IPDPs will be affected by drift shell splitting due to the fact that they are generated by particles that will undergo drift shell splitting, Pi1B waves are not beholden to particle motion and will propagate across the magnetic field cleanly before coupling to field lines.

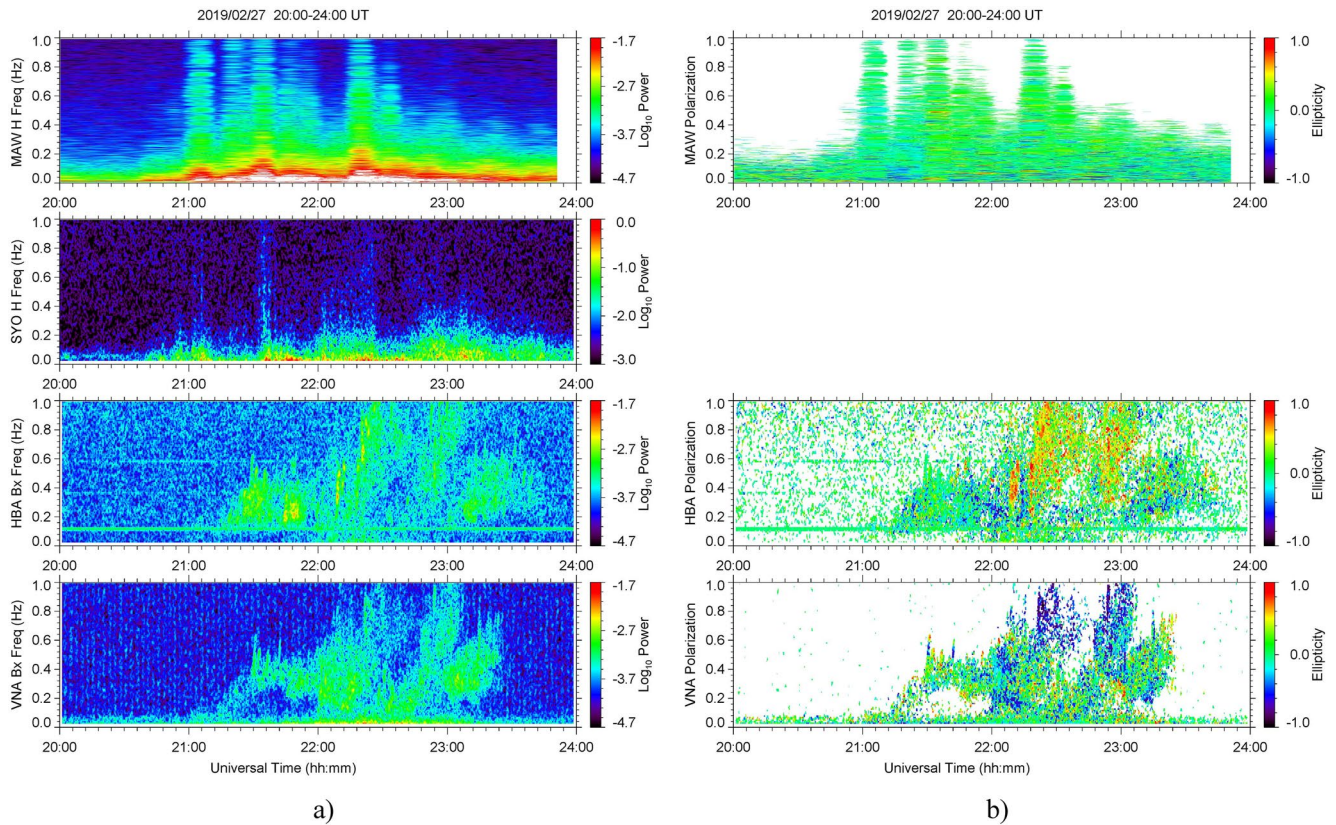


Figure 2. Ground magnetometer (a) spectrograms and (b) polarization analysis for the 27 February 2019 event at MAW, SYO, HBA, and VNA stations respectively (note: SYO polarization is not plotted for reasons discussed in the text). Frequencies between 0 and 1 Hz are plotted on the y axis and UT times between 2000 UT and 2400 UT are plotted on the x axis. The color bar indicates (a) log power and (b) polarization ellipticity, with red reflecting right-handed polarization and blue reflecting left-handed polarization. MAW and SYO data are in HDZ coordinates, with the H coordinate plotted. HBA and VNA data are in XYZ coordinates, with the X coordinate plotted. IPDPs are observed at HBA and VNA (-62.2 and -60.6 CGM lat.) Near-simultaneous Pi1Bs are observed at MAW and SYO (-70.4 and -66.5 CGM lat.).

In situ data from Van Allen Probe A for the February event are plotted in Figure 4. The top panel shows spectrograms of EMFISIS magnetic field data. At 2130 UT, while probe A is in conjunction with SYO, there is part of an EMIC wave, followed by Pi1B bursts. The bottom panel shows RBSPICE H+ flux data between 45 and 598 keV. There are clear proton injection spikes at 2123, 2153, and 2230 UT, all between 100 and 200 keV. The HOPE H+ flux data were not available for this event, but they are included for the March event.

In situ data from Van Allen Probe B for the March event are plotted in Figure 5. Pi1B waves are less apparent than in the previous case study, although there is some low frequency bursty activity between 1930 and 2000 UT. EMIC waves are apparent between 2100 and 2200 UT. The RBSPICE data show proton injection spikes most noticeably at around 2100 and 2130, and less obviously at 1930 and 2230 UT. The HOPE data are plotted in the bottom panel mainly for completeness as the injections are largely at energies above the range of the HOPE instrument, although there is a small range of energies where these instruments overlap that align in both spectrograms and with the EMIC waves.

In both the February (Figure 4) and March (Figure 5) events, EMIC waves are observed from EMFISIS and proton injections are observed from RBSPICE. As is typical for IPDP events, the rising tone is not apparent from the in situ space perspective. There are Pi1B waves visible in the February event nearly simultaneous with the EMIC waves. There are also intermittent wave bursts visible in the March event, but they precede the EMIC waves and are not within the gyrofrequency bands.

As anticipated from Figure 1, the resulting events are temporally observed first at MAW and SYO, then at VNA and HBA, and finally at the Van Allen Probes. The observations of IPDPs, Pi1B waves, and proton injections for

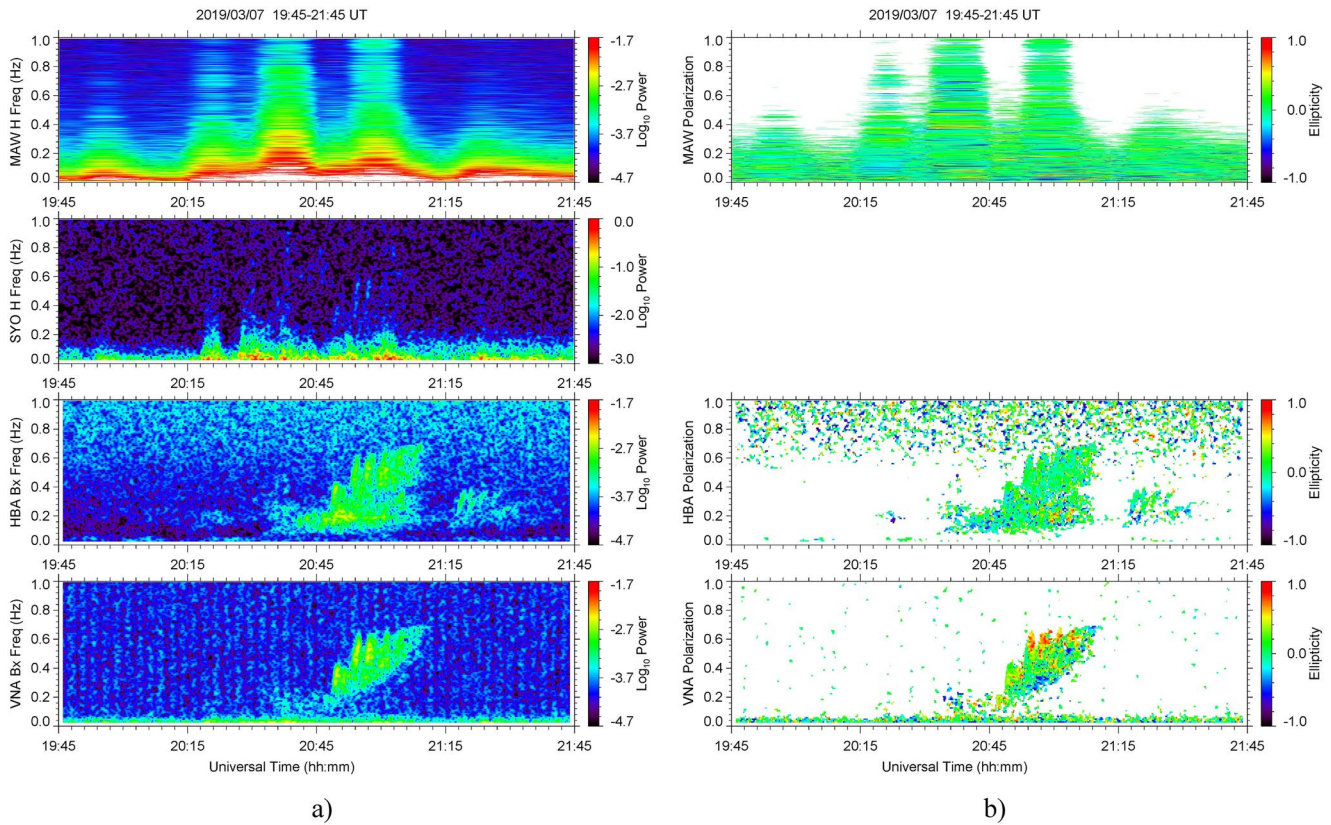


Figure 3. Ground magnetometer (a) spectrograms and (b) polarization analysis for the 7 March 2019 event. Figure is plotted with the same parameters as Figure 2.

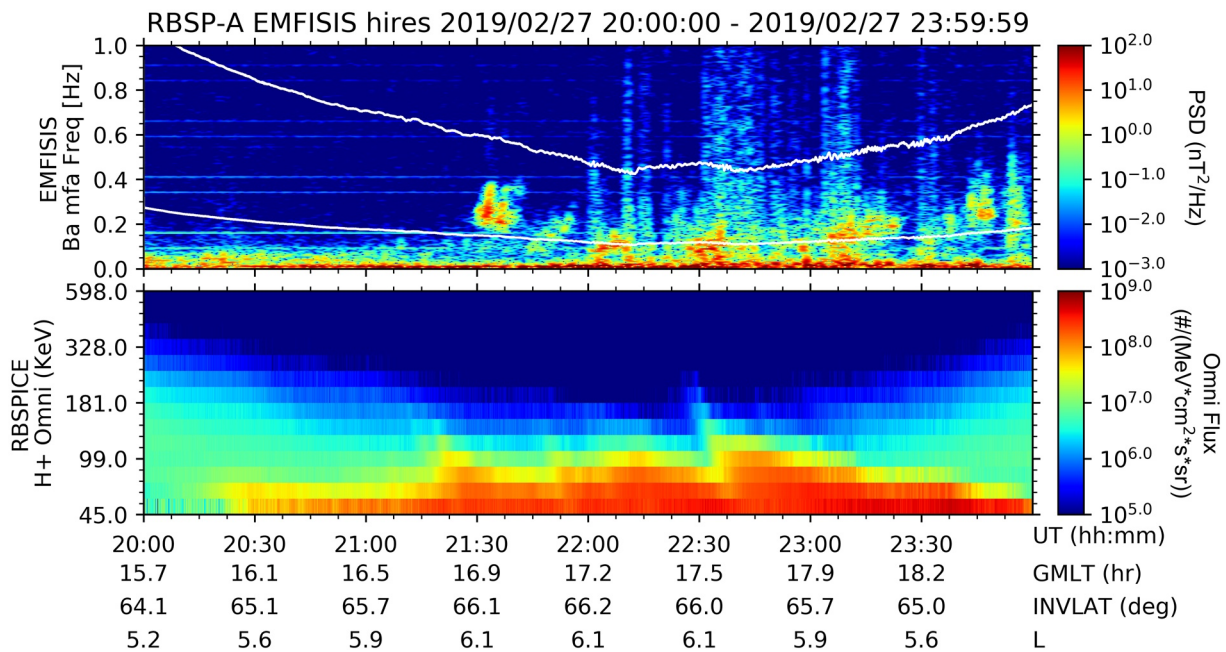


Figure 4. EMFISIS and RBSPICE data from Van Allen Probe A for the 27 February 2019 event. EMFISIS data is plotted in panel one and shows spectrograms of the magnetic field data between 0 and 1 Hz. The white lines are indicative of the gyrofrequencies for He+ (top) and O+ (bottom). RBSPICE data is plotted in panel two and shows H+ Omni fluxes between 45 and 598 keV. The x axis includes UT, GMLT, INVLAT, and L shell.

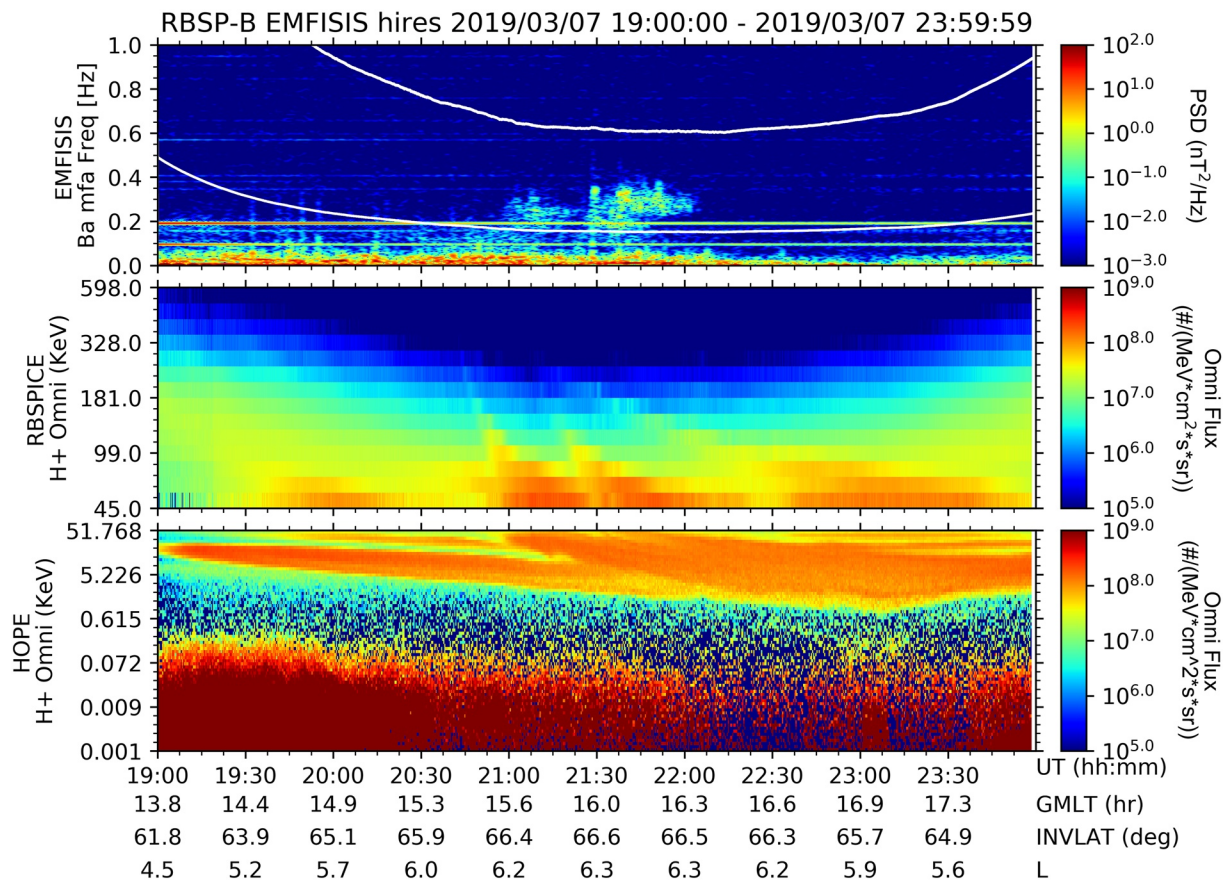


Figure 5. EMFISIS, RBSPICE, and HOPE data from Van Allen Probe B for the 7 March 2019 event. EMFISIS and RBSPICE data are plotted as per Figure 4. HOPE data is plotted in panel three and shows H+ Omni fluxes between 0 and 52 keV.

both case studies will provide injection region boundary conditions and points of comparison for the simulations in the next section.

4. Simulation Results

In this section, we present the results of the preliminary and final simulations. The plasmopause was used as the wave generating region for the IPDPs in these preliminary simulations. The shape of the plasmopause was obtained using the plasmopause test particle (PTP) model (Goldstein et al., 2005, 2014, 2019). This model, which is an adaptive model that has reproduced the plasmopause and the plasmaspheric plumes with good agreement with observations in past studies, utilizes ensembles of cold test particles subject to $E \times B$ drift to resolve the shape of the plasmopause. The model uses the electric field of the solar wind E_{SW} and the K_p index to determine the inner magnetospheric electric field, where the electric field of the solar wind is calculated via $E_{SW} = V_{SW}B_{Z,IMF}$ using OMNI data. Figure 6 shows E_{SW} , K_p , and the resulting shape of the plasmopause acquired from this model. 2100 UT and 2015 UT were chosen to align with the start time of the Pi1Bs observed by the ground stations for the February and March events, respectively (note: Figure 6 shows a time of 2010 UT rather than 2015 UT due to the 10 min timing increments that particular visualization used.)

The results of the preliminary simulation for 121 keV particles as subject to drift shell splitting are showcased in Figure 7. This preliminary simulation assumes that there is a single injection point for the particles that leads to IPDP generation and that the plasmopause is the location where the IPDPs are generated. As these injected protons cross the plasmopause into the plasmasphere, they introduce a temperature anisotropy via the perpendicular energy of the injected particles. For particles with $T_{\perp} > T_{\parallel}$ this should lead to the generation of IPDP waves. These particles have a pitch angle dependence that should cause them to undergo drift shell splitting. This

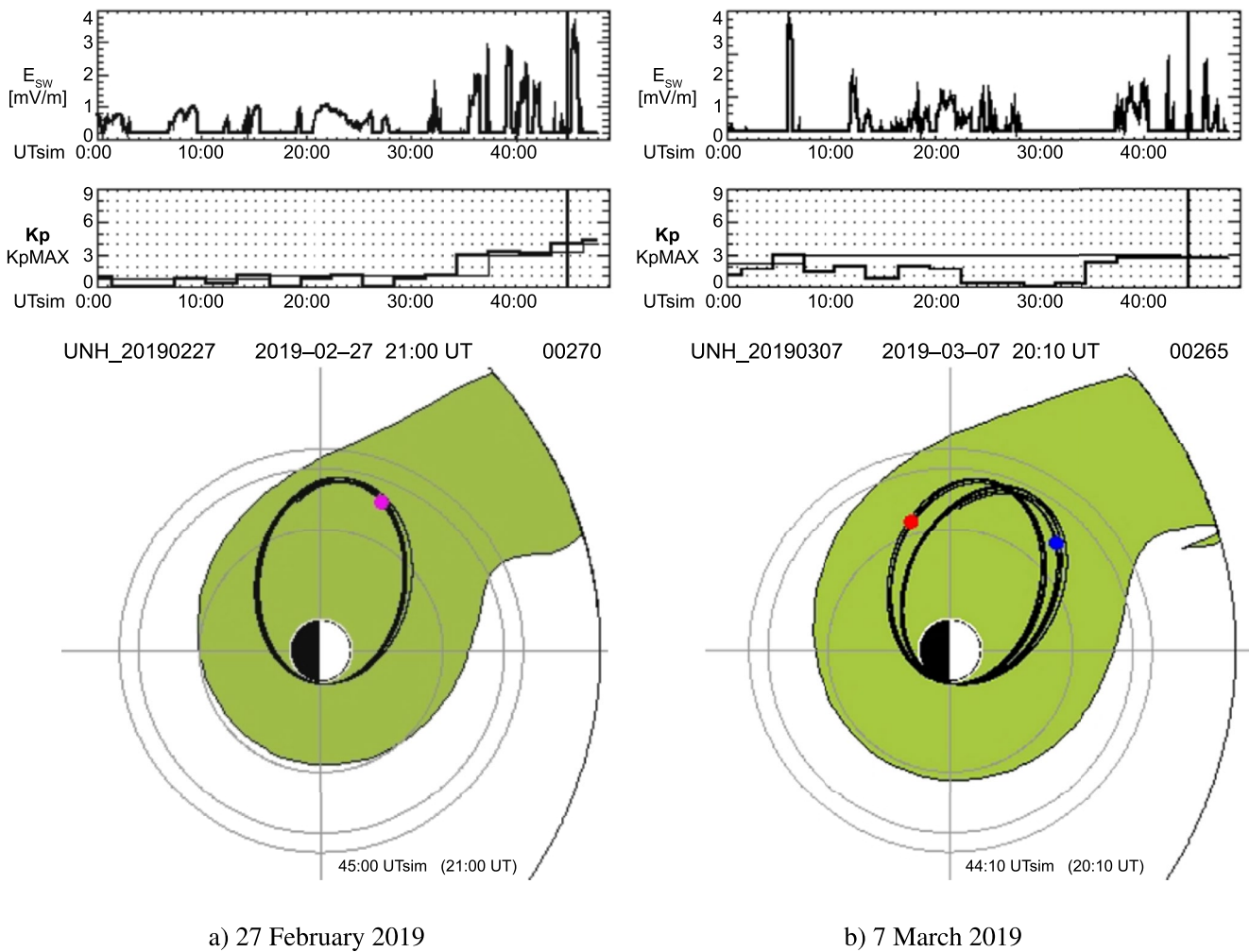


Figure 6. A model of the plasmopause location on: (a) 27 February 2019 at 2100 UT with the Van Allen Probe A orbit overlaid; (b) 7 March 2019 at 2010 UT with the Van Allen Probe A (pink and red) and Van Allen Probe B (blue) orbits overlaid. The top panel displays the input electric field of the solar wind E_{SW} and the second panel displays the K_p index for both events. Going radially outward, the gray circles represent 4 Re, 6 Re, and geostationary orbit respectively. The sun is located to the right.

simulation was based on the dipole + TS05 model with a 0° tilt angle. The simulation solves the Lorentz force equation using a Runge–Kutta sixth order algorithm.

A dipolar magnetic field strength has an L shell dependence such that

$$B(\lambda, L) = \frac{B_E}{L^3} \frac{(1 + 3\sin^2 \lambda)^{1/2}}{\cos^6 \lambda} \quad (1)$$

where B_E is the magnetic field strength at the equator and λ is geomagnetic latitude. This demonstrates that particles that arrive at lower L-shells should correspond to EMIC waves generated at higher frequencies. Additionally, particle gyrofrequency depends on B such that

$$\omega_c = \frac{qB}{m} \quad (2)$$

where q is the charge of the particle and m is the mass of the particle. Combining these equations and folding in the non L variables to the arbitrary operator ξ , the gyrofrequency will have an inverse relationship with L as

$$\omega_c = \frac{\xi}{L^3} \quad (3)$$

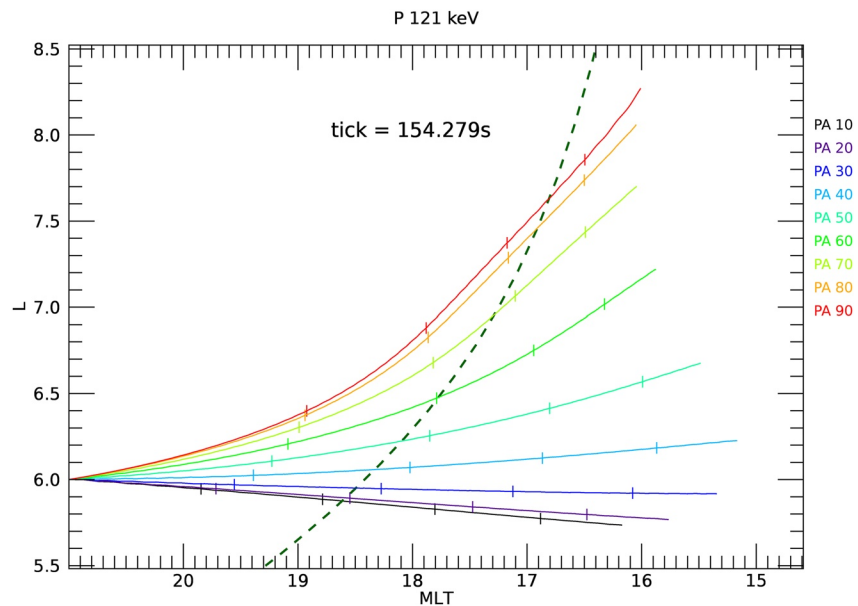


Figure 7. A model of the drift shell splitting that 121 keV protons of different pitch angles undergo. As the pitch angles become less parallel, their trajectories diverge into higher L-shells. The dashed line represents the location of the plasmopause at 2100 UT, as indicated by the PTP model in Figure 6. The presented figure assumes an injection location in the pre-midnight sector at $L = 6$ and an injection time of 2100 MLT. The tickmarks indicate time from injection in intervals of 154.3 s, which is an arbitrary interval length. Models with varying boundary conditions and models for different energies are available upon request.

It was initially thought that the drift shell splitting may contribute to the frequency dispersion of IPDP waves observed on the ground, and that this simple simulation would be sufficient to analyze the effect of drift shell splitting overall. However, as shown in Table 2, the frequency actually decreased over time. It was therefore necessary to simulate particle trajectories using a full injection front rather than a single injection point.

The final simulations were based on the geomagnetic activity-dependent injection boundary model suggested by Mauk and McIlwain (1974). This model estimates the position and shape of a low-energy substorm-injected plasma boundary on the night side as a function of K_p such that the boundary position L_b is:

$$L_b = \frac{122 - 10K_p}{LT - 7.3} \quad (4)$$

For our simulations, K_p was equal to 3. The starting locations of the particles along the injection boundary were evenly spaced with 1 hr MLT intervals. For the February event, they were evenly spaced between 20 and 2 MLT. For the March event, they were evenly spaced between 21 and 2 MLT. From the injection boundary, these simulations traced particle paths by solving the guiding-center averaged equation of motion using a Runge–Kutta sixth order algorithm. The background magnetic field was provided by the TS05 model.

An example of the simulation run for the February event is shown in Figure 8. From these trajectories, the arrival times in seconds to the MLT of the ground stations HBA and VNA was determined. The arrival MLT for HBA was set to 18.86, and the arrival MLT for VNA was set to 18.5. The generated frequencies were then calculated using

$$f = \frac{qB}{2\pi m} \quad (5)$$

where B was provided by the TS05 model. From Summers and Thorne (2003), the dispersion relations for L-mode EMIC waves in a multi ion plasma are

Table 2
The Rough L-Dependent Gyrofrequencies of the Simulated Particles for Each Pitch Angle in Figure 7, Arranged in Order of Ascending Arrival Time

Arrival time (s)	Pitch angle (°)	Arrival location (L shell)	Gyrofrequency (Hz)
262	30	5.95	$\xi \times 4.74e-3$
262	40	6.0	$\xi \times 4.62e-3$
278	50	6.2	$\xi \times 4.19e-3$
308	60	6.5	$\xi \times 3.64e-3$
308	20	5.9	$\xi \times 4.86e-3$
339	10	5.9	$\xi \times 4.86e-3$
401	70	6.9	$\xi \times 3.04e-3$
525	80	7.5	$\xi \times 2.37e-3$
540	90	7.6	$\xi \times 2.27e-3$

Note. For simplicity, ξ is an arbitrary operator that encompasses charge, mass, equatorial magnetic field, and geomagnetic latitude. Overall, as arrival time increases, ω decreases, which is the opposite of what is necessary for a wave to be considered an IPDP.

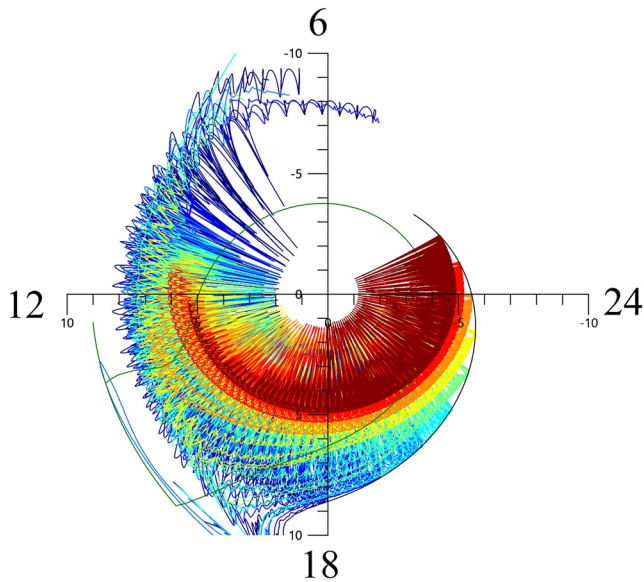


Figure 8. An example of the simulation for 268 keV showcasing the full particle trajectories from the injection boundary. The injection boundary is represented by the black line. Each color corresponds to evenly spaced starting locations in MLT, with the topmost trajectory (red) corresponding to an MLT of 2 and the bottommost trajectory (dark blue) corresponding to an MLT of 20. Each color is composed of 8 lines that correspond to pitch angles between 20° and 90° with 10° intervals. Though it is not explicitly used as the wave generating area in these simulations, the plasmopause location is shown in green, and it is clear from this plot that simulated particles from all starting locations along the injection boundary will cross the plasmopause.

a function of the wave's real frequency normalized by the local magnetic field intensity. This normalized frequency can be presented as ω/Ω_p , where Ω_p is the local proton gyrofrequency. The simulations presented here are normalized by a factor of 0.12, which came from normalizing the observed frequency at the Van Allen probes, approximately 0.3 Hz, by the local proton gyrofrequency. While it would be possible to normalize the wave frequency to the equatorial H+ gyrofrequency, the Van Allen Probe observations were near enough to the equator that this adjustment would not significantly change the simulations. Due to the ambiguous nature of the local proton gyrofrequency in these simulations, the normalization factor of 0.12 was not calculated quantitatively but rather chosen due to how well it modified the simulations to match the ground observations.

To compare the simulations with the observations, the slopes of the observed IPDPs were approximated as per Figure 9. These slopes were then overplotted with the simulation results to compare the IPDP frequency–time characteristics and durations.

Simulated particle arrival times for 30, 54, 81, 121, 180, and 268 keV energies are plotted in Figures 10 and 11. The simulations were run using pitch angles between 20° and 90° in 10° intervals. 10° pitch angles were excluded due to not being sufficiently perpendicular for IPDP generation. Each color in these figures indicates the starting point in MLT of the particle on the injection boundary in evenly spaced 1 hr MLT intervals, and the colors are consistent with Figure 8. Each symbol represents the result of a simulation for one pitch angle, and sets of pitch angles for a given starting MLT tend to be mostly horizontally aligned in arrival time with only a slight increase in frequency over time. The arrival time in seconds for each pitch angle in the 268 keV simulations is shown in Tables 3 and 4. While this shows that there is a general trend that higher pitch angles have earlier arrival times, the arrival time ordering is somewhat complex. For ease of comparison with the

observational data, the black lines in Figures 10 and 11 represent the slopes of the observed IPDPs as depicted in Figure 9.

Comparing the slope and duration of the observations via the black line in Figures 10 and 11 to the slope and duration of the simulated arrival times, it is clear there is an energy dependence such that at lower energies, the arrival times are significantly higher than at higher energies. The simulations for 81 keV are most accurate to the observations for both events. For the March event, the slope of the observed IPDP is 0.015 Hz/min and the simulations for 81 keV have a slope of 0.018 Hz/min. For the February event, the slope of the observed IPDP is 0.026 Hz/min and the simulations for 81 keV also have a slope of approximately 0.026 Hz/min. This shows that this modeling method is valid for reproducing the frequency–time characteristics of the IPDP, and that it can be used to evaluate the contribution of drift shell splitting to the generation of IPDPs. However, it should be noted that while the slopes match well, it is visibly apparent that the frequency range of the simulations is much lower than that of the observations (on the order of 0.2–0.4 Hz difference).

While different pitch angles contribute a slight increase in frequency to the IPDPs, most of the frequency change in the simulations comes from changes in the starting point on the injection boundary. It is clear from these simulations that the frequency change of the IPDPs in these simulations is therefore dominated by injection boundary effects. However, the pitch angle inclusion adds a horizontal spread to the time–frequency characteristics that would otherwise be missing. Additionally, as the MLT on the injection boundary increases, the drift shell splitting leads to a greater horizontal spread in the time–frequency dependence. This results in a somewhat triangular shape in the time–frequency characteristics for the IPDPs, with less horizontal spread at lower frequencies, and greater horizontal spread at higher frequencies. This is all consistent with the observations in Figures 2 and 3.

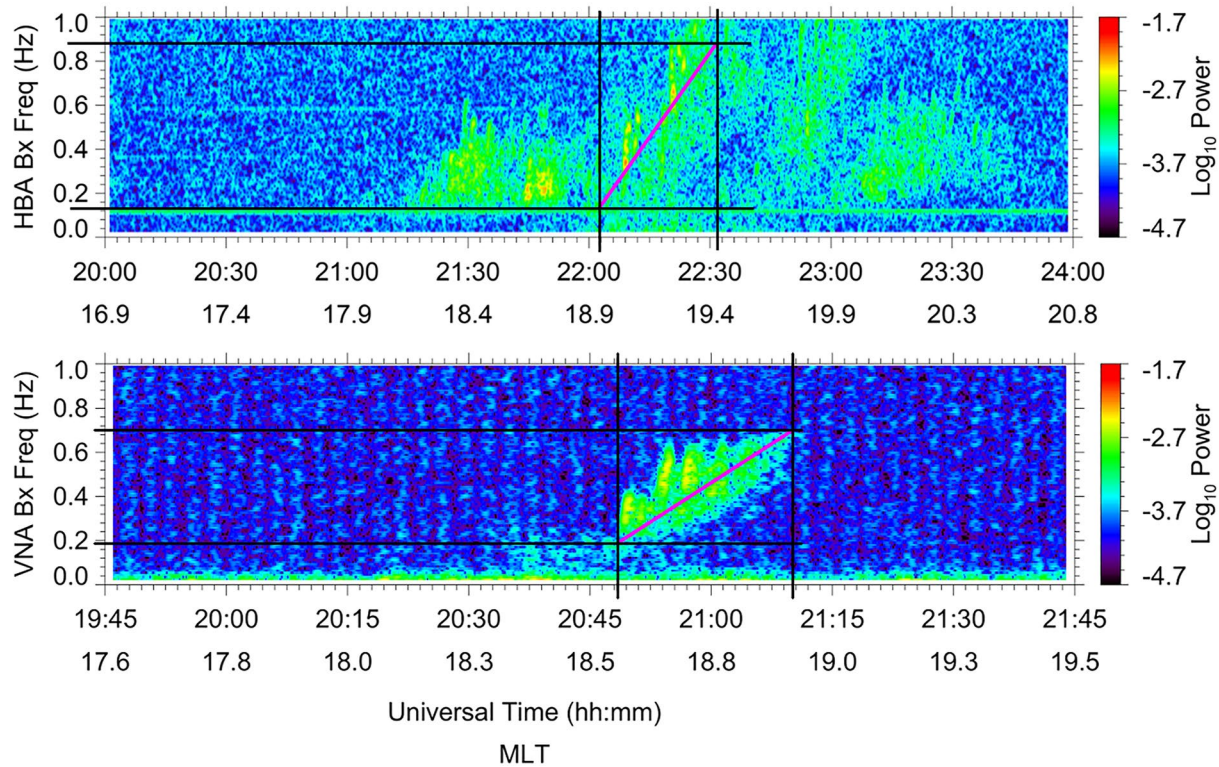


Figure 9. The portions and slopes of the observed IPDP events used to compare to the 27 February 2019 simulations (top) and the 7 March 2019 simulations (bottom).

5. Discussion

The simulations were based on the model described by Mauk and McIlwain (1974) and the results in Søråas et al. (1980). In Søråas et al. (1980), it was shown that IPDP events were associated with increased fluxes of 40–60 keV protons injected near the plasmopause in the equatorial plane during substorms. Our observations are consistent with this, albeit with slightly different energy ranges. As shown in Figures 4 and 5, we observed increased fluxes in the range of 45–181 keV protons. Søråas et al. (1980) developed a model based on Mauk and McIlwain (1974) to explain the relationship between IPDPs and substorms. Per this model, at substorm onset, ring current protons are injected deep into the nightside magnetosphere covering a certain region in L and MLT. The inner edge of the proton population follows the Mauk and McIlwain (1974) injection boundary. Protons drift azimuthally westward and generate ion cyclotron waves in a certain L interval at/inside the plasmopause. The frequency-time dispersion of the IPDP waves are attributed mainly to the L-dependent drift velocity of protons in a narrow energy band.

Similar to the Søråas et al. (1980) model, we used Mauk and McIlwain (1974) and simulated the trajectories of protons at narrow energy bands. In this study, each simulation used one energy. The Søråas et al. (1980) model accounts for the rising frequency of the IPDP waves when observed from the ground by noting that protons arrive earlier at higher L-shells within the wave generation region at specific longitudes, and that because local proton gyrofrequency at lower L shells are larger than at higher L shells, there will be a rise in frequency with time. We arrive at a similar conclusion, where the various starting MLTs on the injection boundary trace out the time-frequency dependence of IPDP waves. While our initial model only accounted for a single injection point, the modified simulations using a full injection front produced the correct time-frequency dependence for the wave. While the Søråas et al. (1980) model predicted general trends that have been found by statistical analysis of IPDP events and accounts for constant frequency observed by satellites during IPDPs, it did not include the effects of drift shell splitting which naturally arise from an asymmetric dipolar magnetic field.

As mentioned in the previous section, these simulations assumed that the normalized wave frequencies were the same over a wide L region, which is valid under the condition that waves are excited by particles with one dominant energy and have similar background plasma conditions. In Figure 10, simulations for 81 keV

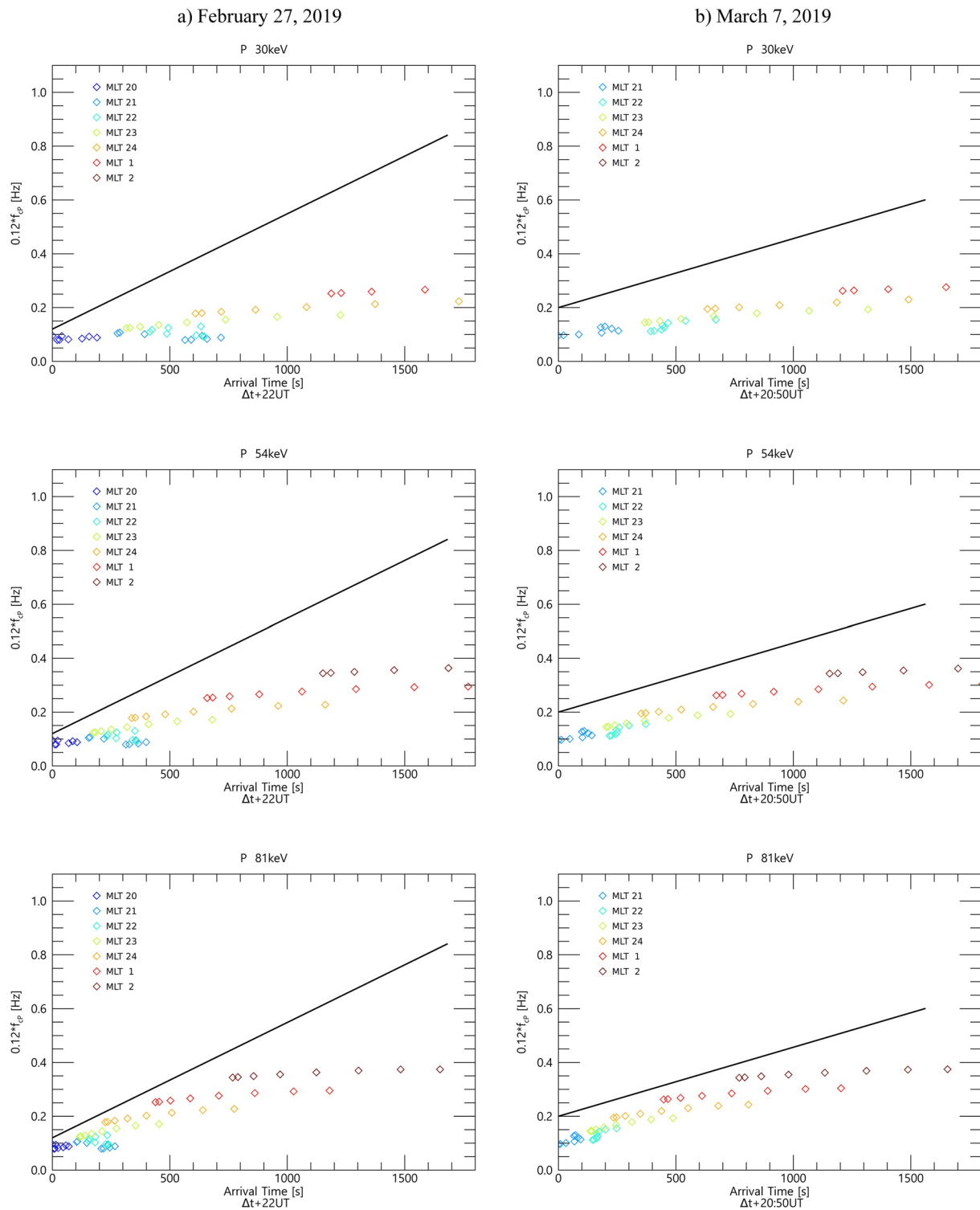


Figure 10. Model results for 30, 54, and 81 keV particles. Simulations for the February event are in the left column, and simulations for the March event are in the right column. The colors indicate MLT arrival time along the injection boundary. The black lines represent the slope of the observed IPDPs on the ground (for the February event, this slope is specifically from the second interval of the larger IPDP event).

are most similar to the ground observations. This may indicate that 81 keV was the dominant energy for these events. However, while these simulations were mostly consistent with observations, the energy dependence of the slope and the duration were not fully able to be inferred from this model. Additionally, the frequency range

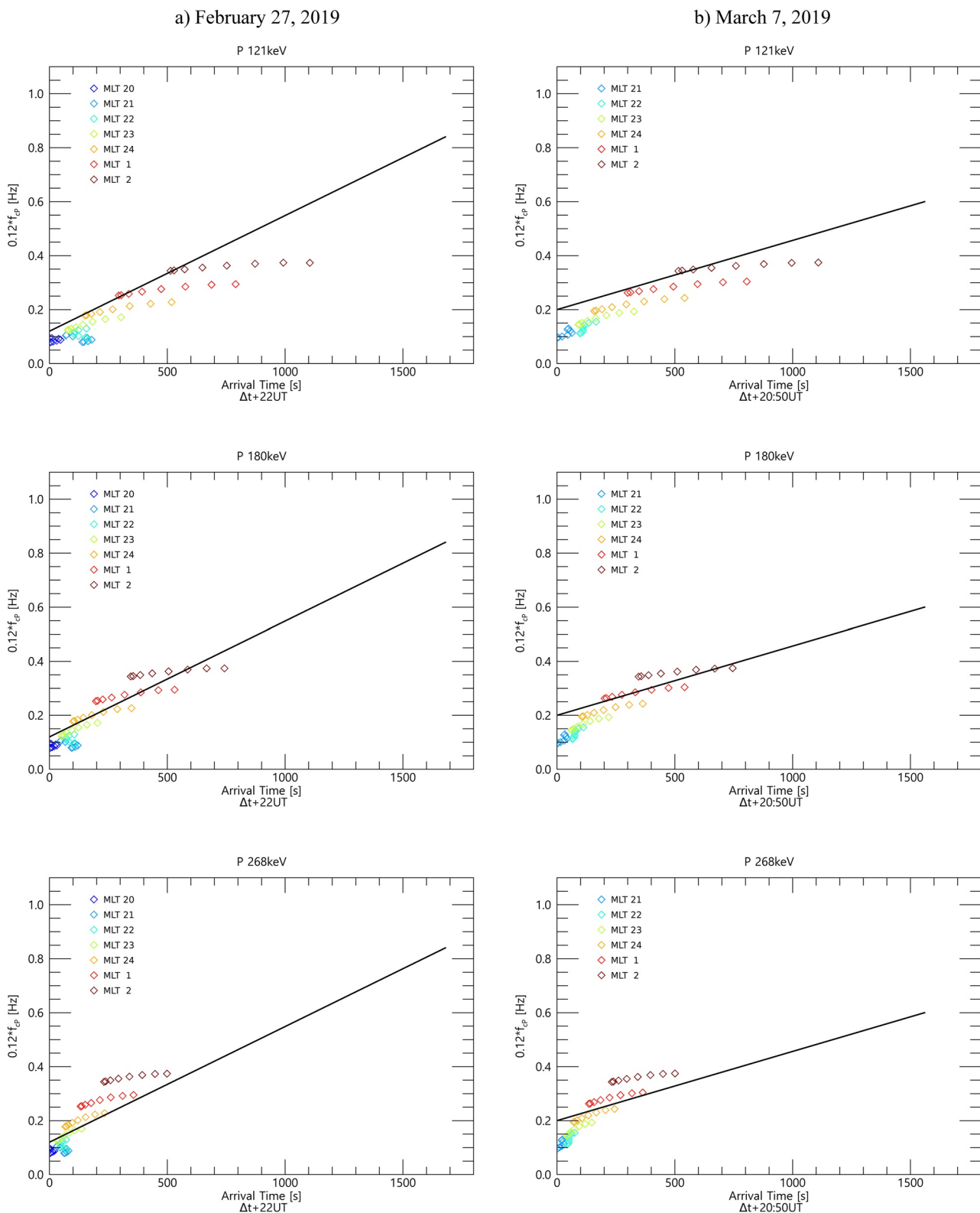


Figure 11. Model results for 121, 180, and 268 keV particles. Simulations for the February event are in the left column, and simulations for the March event are in the right column. The colors indicate MLT arrival time along the injection boundary. The black lines represent the slope of the observed IPDPs on the ground (for the February event, this slope is specifically from the second interval of the larger IPDP event).

Table 3

The Arrival Time in Seconds for Each Pitch Angle Interval From Each MLT Along the Injection Boundary for 268 keV Particles on 27 February 2019

MLT	PA20	PA30	PA40	PA50	PA60	PA70	PA80	PA90
20	51.0	55.7	68.6	71.8	64.5	57.9	53.7	52.6
21	83.5	82.7	96.4	124.0	131.8	124.6	116.7	113.6
22	121.5	106.3	98.9	98.4	106.9	120.5	123.5	122.4
23	187.7	157.6	133.2	114.9	101.4	92.4	87.4	85.7
24	284.8	244.3	204.4	171.7	147.4	130.9	121.6	118.5
1	407.5	361.3	311.2	264.8	228.0	202.6	188.0	183.2
2	549.7	498.9	444.7	390.4	343.7	309.5	289.3	282.5

Note. While overall arrival time is earlier for higher pitch angles, there is some complexity to the arrival time structure. While the specific arrival times change across simulated energies, the ordering does not.

of the simulations was truncated compared to observations. It is possible that different simulations that did not rely upon a dominant energy would more closely replicate ground observations. Our simulations also only account for injection boundary effects, and do not factor in any of the more complex physics that may occur over the course of the particle trajectories. However, this study did not seek to recreate the time–frequency characteristics of the observed IPDPs, but rather to identify if drift shell splitting could contribute to the time–frequency characteristics of IPDPs.

The inclusion of drift shell splitting was reflected in the differences in the simulation across different pitch angles. It can be seen in Figures 10 and 11 and Tables 3 and 4 that particles with different pitch angles have different arrival times, adding a horizontal component to the simulated IPDPs. Additionally, in both the simulations and observations, the portions of the IPDPs at higher frequencies lasted for longer durations than the portions of the IPDPs at lower frequencies, leading to a triangular shape in the time–frequency characteristics. It can ultimately be inferred from this that drift shell splitting plays a minor but non-zero role in IPDP generation by affecting the time–frequency characteristics.

6. Conclusions

In this study, we investigated simultaneous observations of substorm onset related IPDP-type EMIC waves and Pi1B ULF waves. This research follows the work done by Søråas et al. (1980) and is motivated by understanding the effects of drift shell splitting on the generation, propagation, and observation of IPDP waves. We used high quality searchcoil magnetometer data from a set of four Antarctic ground stations (HBA, VNA, SYO, and MAW) as well in situ space data from EMFISIS, RBSPICE, and HOPE aboard the Van Allen probes. We observed IPDPs at HBA and VNA and Pi1Bs at SYO and MAW for both events. We also observed proton injections from substorm onset using the Van Allen probes.

1. Using the injection boundary model from Mauk and McIlwain (1974), we simulated the trajectories of substorm-injected protons along an injection boundary as subject to drift shell splitting.
2. In these simulations, the overall frequency increase of the IPDPs were dominated by injection boundary effects; these findings were mostly consistent with our ground observations.
3. The inclusion of drift shell splitting introduced a slight horizontal component to the time–frequency dependence of the IPDPs such that at higher frequencies the duration of the IPDP was longer than at lower frequencies.
4. We conclude that drift shell splitting mainly influences the shape of the IPDPs as observed from the ground.

Table 4

The Arrival Time in Seconds for Each Pitch Angle Interval From Each MLT Along the Injection Boundary for 268 keV Particles on 7 March 2019

MLT	PA20	PA30	PA40	PA50	PA60	PA70	PA80	PA90
21	128.8	126.9	132.1	135.3	127.3	116.4	109.2	106.8
22	181.6	167.3	159.0	156.5	157.3	156.0	152.4	150.8
23	254.1	226.1	201.3	180.9	165.4	155.2	149.7	148.0
24	351.1	312.5	273.6	239.5	212.2	192.9	181.6	177.8
1	470.4	424.7	376.1	329.8	291.5	263.9	247.6	242.3
2	607.5	556.5	503.1	449.6	402.9	367.8	346.5	339.5

Data Availability Statement

Data from the MICA magnetometer array are available at http://mir1.unh.edu/ulf_status.html. The Mawson riometer data were provided by the Australian Space Weather Service and the Australian Antarctic Division. Data from the induction magnetometer and imaging riometer at Syowa are available at <http://iugonet0.nipr.ac.jp/data/>. The Mawson magnetometer data were provided by the Australian Bureau of Meteorology Space Weather Services and are available at https://www.sws.bom.gov.au/World_Data_Centre/1/2. The geomagnetic Kp index was retrieved from GFZ Potsdam (Matzka, Jürgen; Bronkalla, Oliver; Tornow, Katrin; Elger, Kirsten; Stolle, Claudia (2021): Geomagnetic Kp index. V. 1.0. GFZ Data Services. <https://doi.org/10.5880/Kp.0001>).

Acknowledgments

The work at the University of New Hampshire was supported by NSF under grants NSF awards 2133897, 2129040, and 1745041. The work at the New Jersey Institute of Technology (NJIT) was supported by NSF under grant AGS-2133837 and the NASA Van Allen Probes RBSPICE instrument project, as supported by JHU/APL Subcontract No. 131803 to NJIT under NASA Prime Contract No. NNN06AA01C. The work of K.-H. Kim was supported by project PE22020 of the Korea Polar Research Institute. The work at Augsburg University was supported by NSF under grant AGS-2013648. The database construction for the ground-based observational data at Syowa has been partly supported by the IUGONET (Inter-university Upper atmosphere Global Observation NETwork) project (<http://www.iugonet.org/index.jsp>) funded by the MEXT. RBH and MAC would like to acknowledge support from the UK Research and Innovation (UKRI-NERC) through National Capability Space Weather Observatory funding (NC-SS SWO). Neumayer III and Kohlen Station in Antarctica are operated by the Alfred Wegener Institute (Alfred-Wegener-Institut Helmholtz-Zentrum für Polar-und Meeresforschung. (2016). Journal of large-scale research facilities, 2, A85. <https://jlsrf.org/index.php/lrf/article/view/152>).

References

- Allen, R. C., Zhang, J.-C., Kistler, L. M., Spence, H., Lin, R.-L., Klecker, B., et al. (2015). A statistical study of EMIC waves observed by Cluster: 1. Wave properties. *Journal of Geophysical Research: Space Physics*, 120(7), 5574–5592. <https://doi.org/10.1002/2015JA021333>
- Arnoldy, R. L., & Lewis, P. B. (1979). Polarization of Pc 1 and IPDP pulsations correlated with particle precipitation. *Journal of Geophysical Research*, 84(A12), 7091–7098. <https://doi.org/10.1029/JA084iA12p07091>
- Arnoldy, R. L., Posch, J. L., Engebretson, M. J., Fukunishi, H., & Singer, H. J. (1998). Pi1 magnetic pulsations in space and at high latitudes on the ground. *Journal of Geophysical Research: Space Physics*, 103(A10), 23581–23591. <https://doi.org/10.1029/98JA01917>
- Bossen, M., McPherron, R. L., & Russell, C. T. (1976). Simultaneous Pc 1 observations by the synchronous satellite ATS-1 and ground stations: Implications concerning IPDP generation mechanisms. *Journal of Atmospheric and Terrestrial Physics*, 38(11), 1157–1167. [https://doi.org/10.1016/0021-9169\(76\)90046-5](https://doi.org/10.1016/0021-9169(76)90046-5)
- Brito, T. V., Halford, A. J., & Elkington, S. R. (2020). Chapter 2 - Ultralow frequency-wave induced losses. In A. N. Jaynes & M. E. Usanova (Eds.), *The dynamic loss of earth's radiation belts* (pp. 29–48). Elsevier. <https://doi.org/10.1016/b978-0-12-813371-2.00002-0>
- Chen, A. J., & Wolf, R. A. (1972). Effects on the plasmasphere of a time-varying convection electric field. *Planetary and Space Science*, 20(4), 483–509. [https://doi.org/10.1016/0032-0633\(72\)90080-3](https://doi.org/10.1016/0032-0633(72)90080-3)
- Cornwall, J. (1965). Cyclotron instabilities and electromagnetic emission in the ultralow frequency and very low frequency ranges. *Journal of Geophysical Research*, 70(1), 61–69. <https://doi.org/10.1029/JZ070i001p00061>
- Fowler, R. A., Kotick, B. J., & Elliott, R. D. (1967). Polarization analysis of natural and artificially induced geomagnetic micropulsations. *Journal of Geophysical Research*, 72(11), 2871–2883. <https://doi.org/10.1029/JZ072i011p02871>
- Goldstein, J., Pascuale, S., & Kurth, W. S. (2019). Epoch-based model for stormtime plasmopause location. *Journal of Geophysical Research: Space Physics*, 124(6), 4462–4491. <https://doi.org/10.1029/2018ja025996>
- Goldstein, J., Pascuale, S. D., Kletzing, C., Kurth, W., Genestreti, K. J., Skoug, R. M., et al. (2014). Simulation of Van Allen probes plasmopause encounters. *Journal of Geophysical Research: Space Physics*, 119(9), 7464–7484. <https://doi.org/10.1002/2014ja020252>
- Goldstein, J., Sandel, B. R., Forrester, W. T., Thomsen, M. F., & Hairston, M. R. (2005). Global plasmasphere evolution 22–23 April 2001. *Journal of Geophysical Research: Space Physics*, 110(A12). <https://doi.org/10.1029/2005ja011282>
- Heacock, R. R. (1967). Two subtypes of type Pi micropulsations. *Journal of Geophysical Research*, 72(15), 3905–3917. <https://doi.org/10.1029/JZ072i015p03905>
- Heacock, R. R. (1971). Spatial and temporal relations between Pi bursts and IPDP micropulsation events. *Journal of Geophysical Research*, 76(19), 4494–4504. <https://doi.org/10.1029/JA076i019p04494>
- Heacock, R. R. (1973). Type IPDP magnetospheric plasma wave events. *Nature Physical Science*, 246, 93–96. <https://doi.org/10.1038/physci246093b0>
- Horita, R. E., Barfield, J. N., Heacock, R. R., & Kangas, J. (1979). IPDP source regions and resonant proton energies. *Journal of Atmospheric and Terrestrial Physics*, 41(3), 293–309. [https://doi.org/10.1016/0021-9169\(79\)90112-0](https://doi.org/10.1016/0021-9169(79)90112-0)
- Jacobs, J. A., Kato, Y., Matsushita, S., & Troitskaya, V. A. (1964). Classification of geomagnetic micropulsations. *Journal of Geophysical Research*, 69(1), 180–181. <https://doi.org/10.1029/JZ069i001p00180>
- Kim, H. (2010). *Development of ground-based search-coil magnetometer systems in the polar regions and studies of ULF Pc 1-2 wave propagation in the ionospheric waveguide (PhD dissertation)*. University of New Hampshire.
- Kim, H., Lessard, M. R., Engebretson, M. J., & Lühr, H. (2010). Ducting characteristics of Pc 1 waves at high latitudes on the ground and in space. *Journal of Geophysical Research: Space Physics*, 115(A9). <https://doi.org/10.1029/2010JA015323>
- Kim, H., Lessard, M. R., Engebretson, M. J., & Young, M. A. (2011). Statistical study of pc1–2 wave propagation characteristics in the high-latitude ionospheric waveguide. *Journal of Geophysical Research: Space Physics*, 116(A7). <https://doi.org/10.1029/2010ja016355>
- Kivelson, M. G., & Russell, C. T. (1995). *Introduction to space physics*. Cambridge University Press.
- Koleszar, T. (1988). *The generation of IPDP micropulsations, with special attention to frequency shift mechanisms (PhD dissertation)*. University of British Columbia.
- Lessard, M. R., Lund, E. J., Jones, S. L., Arnoldy, R. L., Posch, J. L., Engebretson, M. J., & Hayashi, K. (2006). Nature of Pi1B pulsations as inferred from ground and satellite observations. *Geophysical Research Letters*, 33(14). <https://doi.org/10.1029/2006GL026411>
- Lessard, M. R., Lund, E. J., Kim, H. M., Engebretson, M. J., & Hayashi, K. (2011). Pi1B pulsations as a possible driver of Alfvénic aurora at substorm onset. *Journal of Geophysical Research: Space Physics*, 116(A6). <https://doi.org/10.1029/2010JA015776>
- Maltseva, N., Troitskaya, V., Gerazimovitch, E., Baransky, L., Åsheim, S., Hollet, J., et al. (1981). On temporal and spatial development of IPDP source region. *Journal of Atmospheric and Terrestrial Physics*, 43(11), 1175–1188. [https://doi.org/10.1016/0021-9169\(81\)90033-7](https://doi.org/10.1016/0021-9169(81)90033-7)
- Mauk, B. H., & McIlwain, C. E. (1974). Correlation of Kp with the substorm-injected plasma boundary. *Journal of Geophysical Research*, 79(22), 3193–3196. <https://doi.org/10.1029/ja079i022p03193>
- Moldwin, M. B., Howard, J., Sanny, J., Bocchicchio, J. D., Rassoul, H. K., & Anderson, R. R. (2004). Plasmaspheric plumes: CRRES observations of enhanced density beyond the plasmopause. *Journal of Geophysical Research: Space Physics*, 109(A5). <https://doi.org/10.1029/2003JA010320>
- Neudegg, D., Fraser, B., Menk, F., Waters, C., Burns, G., & Morris, R. (2000). Ulf wave attenuation in the high latitude ionospheric waveguide. *Advances in Space Research*, 25(7), 1559–1565. Proceedings of the DO.1 Symposium of COSPAR Scientific Commission D. [https://doi.org/10.1016/s0273-1177\(99\)00668-7](https://doi.org/10.1016/s0273-1177(99)00668-7)
- Pilipenko, V. A., Mazur, N. G., Fedorov, E. N., & Engebretson, M. J. (2008). Interaction of propagating magnetosonic and Alfvén waves in a longitudinally inhomogeneous plasma. *Journal of Geophysical Research: Space Physics*, 113(A8). <https://doi.org/10.1029/2007ja012651>

- Rankin, D., & Kurtz, R. (1970). Statistical study of micropulsation polarizations. *Journal of Geophysical Research*, 75(28), 5444–5458. <https://doi.org/10.1029/JA075i028p05444>
- Ranta, A., Ranta, H., Rosenberg, T. J., Wedeken, U., & Stauning, P. (1983). Development of an auroral absorption substorm: Studies of substorm related absorption events in the afternoon-early evening sector. *Planetary and Space Science*, 31(12), 1415–1434. [https://doi.org/10.1016/0032-0633\(83\)90017-X](https://doi.org/10.1016/0032-0633(83)90017-X)
- Remya, B., Sibeck, D. G., Halford, A. J., Murphy, K. R., Reeves, G. D., Singer, H. J., et al. (2018). Ion injection triggered EMIC waves in the earth's magnetosphere. *Journal of Geophysical Research: Space Physics*, 123, 4921–4938. <https://doi.org/10.1029/2018JA025354C>
- Roederer, J. G. (1967). On the adiabatic motion of energetic particles in a model magnetosphere. *Journal of Geophysical Research*, 72(3), 981–992. <https://doi.org/10.1029/JZ072i003p00981>
- Sagdeev, R. Z., & Shafranov, V. D. (1961). On the instability of a plasma with an anisotropic distribution of velocities in a magnetic field. *Soviet Physics Journal of Experimental and Theoretical Physics*, 3(1), 130–132.
- Søraas, F., Lundblad, J. Å., Maltseva, N. F., Troitskaya, V., & Selivanov, V. (1980). A comparison between simultaneous I.P.D.P. ground-based observations and observations of energetic protons obtained by satellites. *Planetary and Space Science*, 28(4), 387–405. [https://doi.org/10.1016/0032-0633\(80\)90043-4](https://doi.org/10.1016/0032-0633(80)90043-4)
- Summers, D., & Thorne, R. M. (2003). Relativistic electron pitch-angle scattering by electromagnetic ion cyclotron waves during geomagnetic storms. *Journal of Geophysical Research: Space Physics*, 108(A4). <https://doi.org/10.1029/2002ja009489>
- Takahashi, K., Anderson, B. J., Ohtani, S., Reeves, G. D., Takahashi, S., Sarris, T. E., & Mursula, K. (1997). Drift-shell splitting of energetic ions injected at pseudo-substorm onsets. *Journal of Geophysical Research: Space Physics*, 102(A10), 22117–22130. <https://doi.org/10.1029/97JA01870>
- Usanova, M. E., Drozdov, A., Orlova, K., Mann, I. R., Shprits, Y., Robertson, M. T., et al. (2014). Effect of EMIC waves on relativistic and ultra-relativistic electron populations: Ground-based and Van Allen probes observations. *Geophysical Research Letters*, 41(5), 1375–1381. <https://doi.org/10.1002/2013GL059024>